

Supporting Information

**Co-intercalation of Multiple Active Units in Graphene by
Pyrolysis of Hydrogen-bonded Precursors for Zinc–air Batteries
and Water Splitting**

*Yiyin Huang, Qin Liu, Jiangquan Lv, Dickson D. Babu, Wenjing Wang, Maoxiang Wu,
Daqiang Yuan, Yaobing Wang**

Key Laboratory of Design and Assembly of Functional Nanostructures, and Fujian Provincial
Key Laboratory of Nanomaterials, Fujian Institute of Research on the Structure of Matter,
Chinese Academy of Sciences, Fuzhou, Fujian 350002, China
Tel: 0591-22853916; E-mail: wangyb@fjirsm.ac.cn

Table 1. Mass contents of Co in Co@CNG, CoG, D-Co@CN and D-Co@CNG as determined by ICP-OES analysis.

	Content (wt.%)
Co@CNG	3.53
CoG	0.45
D-Co@CN	0.886
D-Co@CNG	3.58



Figure 1. The preparative processes for Co@CNG and D-Co@CNG tri-functional electrocatalyst.

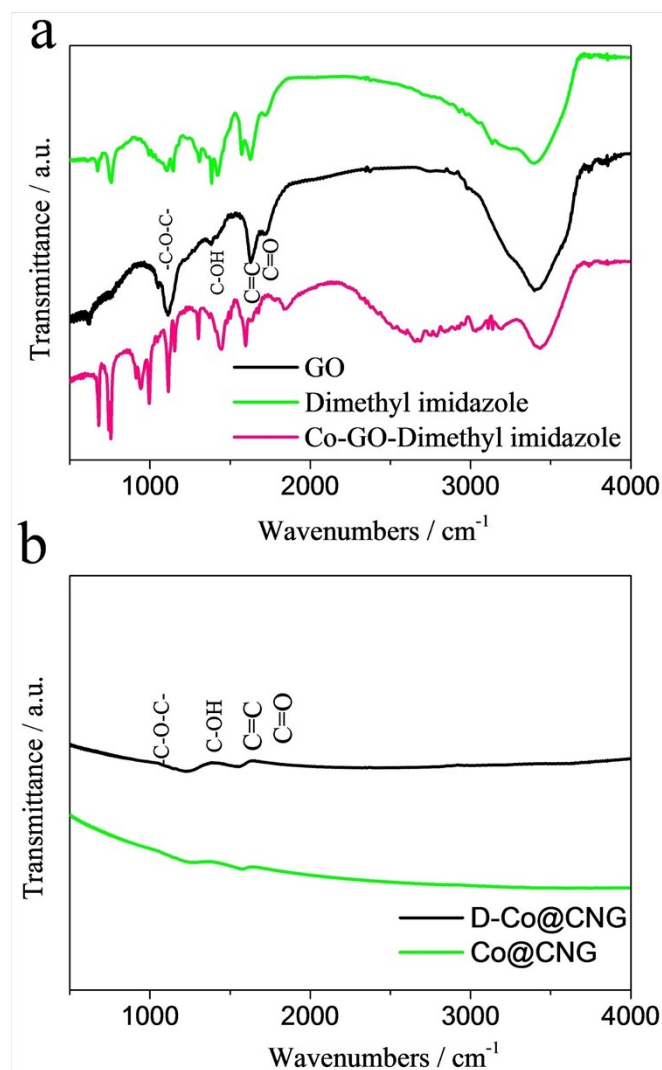


Figure 2. Infrared (IR) spectra of (a) GO, Dimethyl imidazole and Co-GO- dimethyl imidazole, and (b) D-Co@CNG and Co@CNG.

For 2-dimethyl imidazole, the bands in the range of 600–1500 cm⁻¹ corresponds to the stretching and bending modes of the imidazole ring, whereas the band at 1585 cm⁻¹ can be attributed to the stretching mode of C=N bonding in 2-MIM. Besides, the bands at 2930 and 3134 cm⁻¹ are derived from the stretching mode of C-H from the aliphatic chain and the aromatic ring in 2-MIM, respectively. The broad peak in the range of 2500 to 3650 cm⁻¹ was due to stretching vibrations of –NH in 2-MIM and –OH group from absorbed water. For GO, the peaks at 1040 cm⁻¹ (C-O-C), 1220 cm⁻¹

(C-O), 1415 cm^{-1} (C-O-H), 1620 cm^{-1} (C=C), 1732 cm^{-1} (C=O), 3400 cm^{-1} (O-H) can be observed as reported.^{1,2} Besides, the broad peak in the range of 2900 to 3600 cm^{-1} was assigned to stretching vibrations of -OH group in GO. The Co-GO-dimethyl imidazole displays all the characteristic peaks of the solitary counterparts. In addition, the more distinct broad peak centered at 2600 cm^{-1} was probably due to the formation of hydrogen bond between -OH group on graphene oxide and N moieties on 2-MIM.

After pyrolysis, most of the above groups disappear or become less obvious, suggesting the carbonization successfully proceeded.

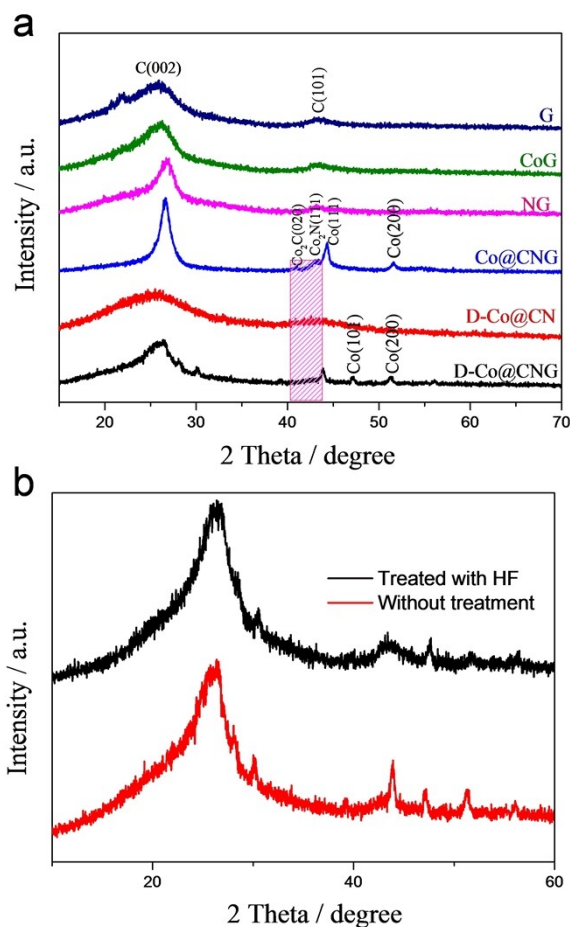


Figure 3. (a) X-ray powder diffraction (XRD) patterns of D-Co@CNG, D-Co@CN, Co@CNG, NG, CoG and G; (b) XRD patterns of D-Co@CNG treated with and without HF.

The peaks at 44.3° , 47.1° and 51.7° correspond to the (111), (101) and (200) planes of Co. The peaks at 41.0° and 42.9° correspond to the (020) of Co_2C and (111) of Co_2N planes, respectively. Some CoO may also exist as its (200) plane is located at ca. 42.4° (JCPDS Nos. 65-2902).

The peaks related to Co species became lower and wider, indicating that the cobalt was partly dissolved. Meanwhile, the remaining Co peaks suggested that the

geometric confinement of part of cobalt nanoparticles within nitrogen-doped carbon shells. These facts revealed the coexistence of various Co species.

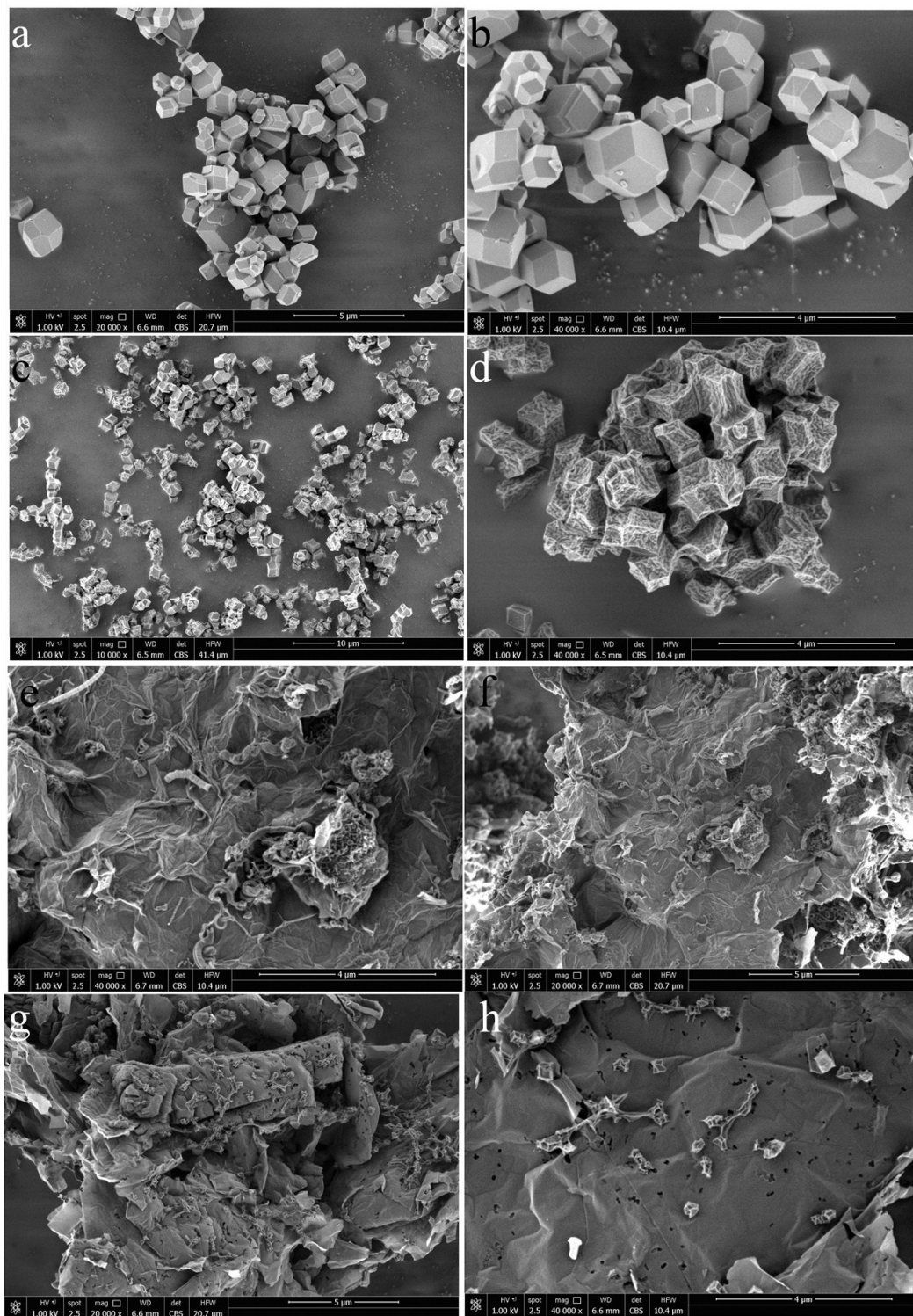


Figure 4. Scanning electron microscopy images (SEM) of (a, b) ZnCo-MOF, (c, d) D-Co@CN, (e, f) Co@CNG and (g, h) D-Co@CNG.

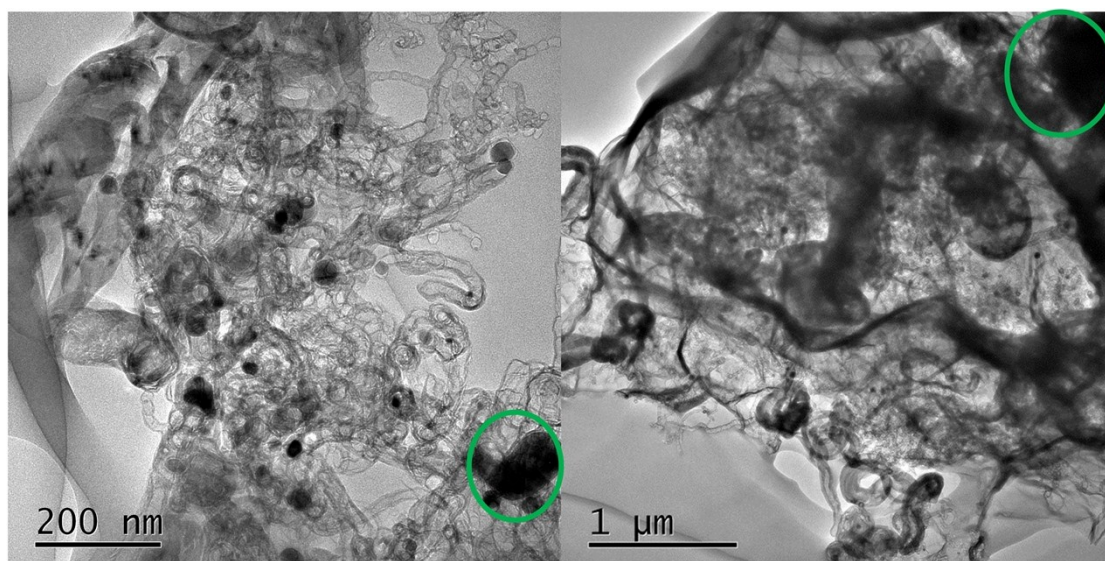


Figure 5. Transmission electron microscopy (TEM) images of Co@CNG.

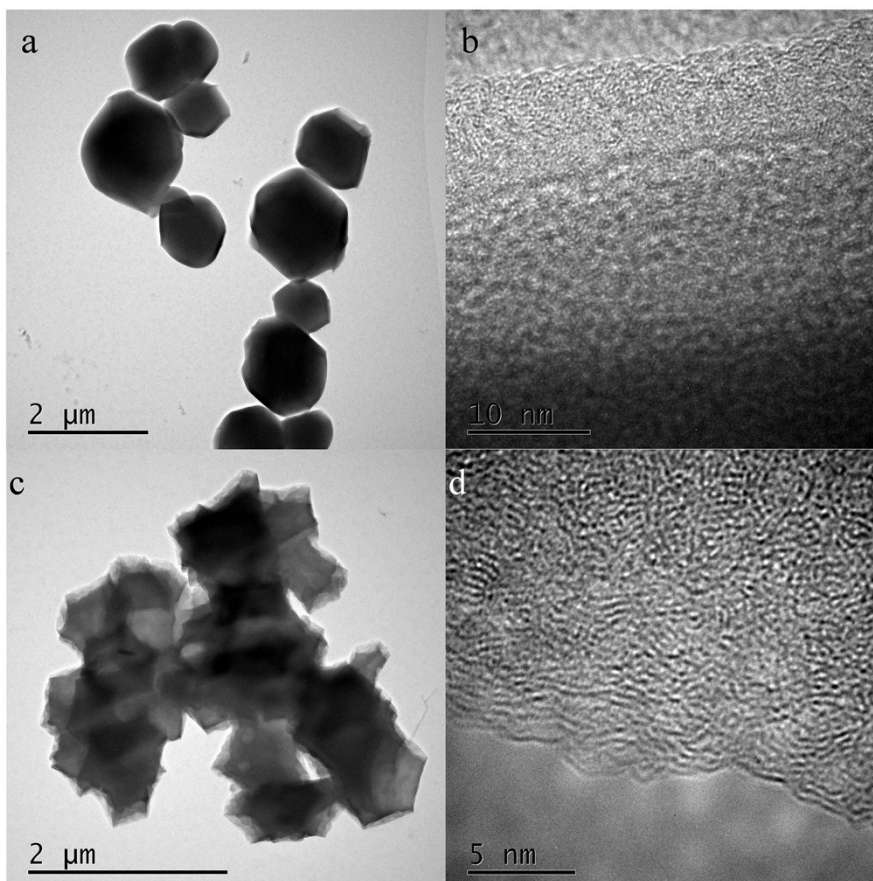


Figure 6. TEM images of (a, b) ZnCo-MOF and (c, d) D-Co@CN.

The $\text{Co}^{2+}/\text{Zn}^{2+}$ metal ions can coordinate with 2-MIM to form metal-organic frameworks analogous to ZIF-8. The morphological characterization is nanopolyhedrons with smooth surfaces and the size ranging from 0.5 to 1.5 μm , as revealed in Fig. 4a, 4b, 6a and 6b. Upon carbonization, the resulting D-Co@NC inherited the overall polyhedron-like morphology (Fig. 4c, 4d, 6c and 6d) with a slight constriction in size (0.6-1.2 μm). Simultaneously, the rough and porous carbon matrices on the surface were observed in the highly magnified SEM, in a sharp contrast with its smooth precursors. The pore-rich architecture of the composite presumably promotes the mass transport process during electrocatalysis. However, agglomerates also occurred on the derived products, counteracting the positive effect brought from porous characteristic.

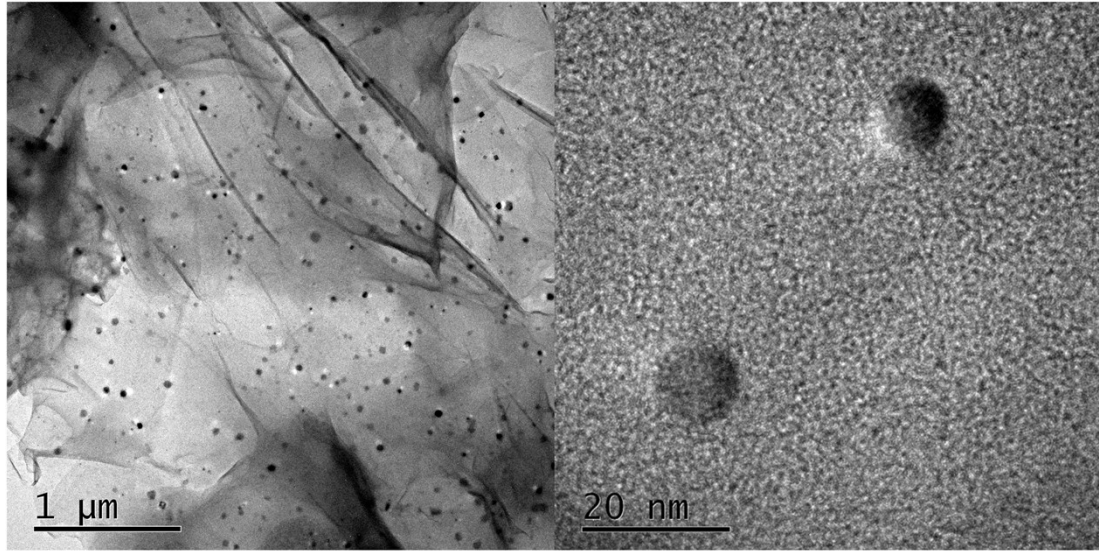


Figure 7. TEM images of D-Co@CNG.

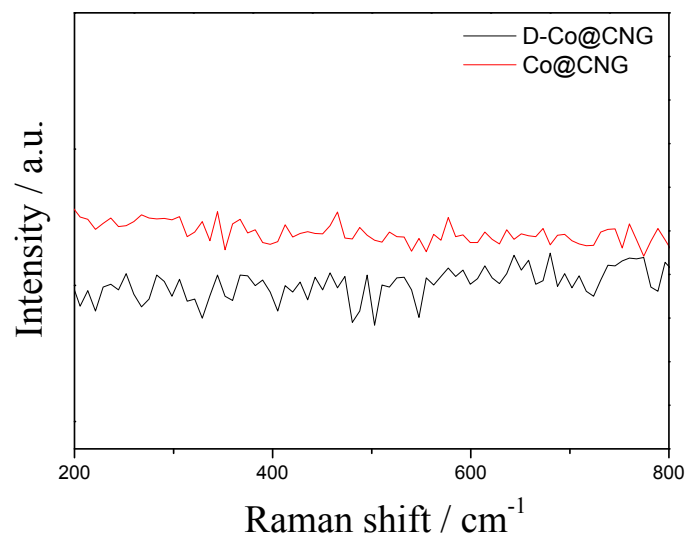


Figure 8. Raman spectra of D-Co@CNG and Co@CNG at low Raman shift.

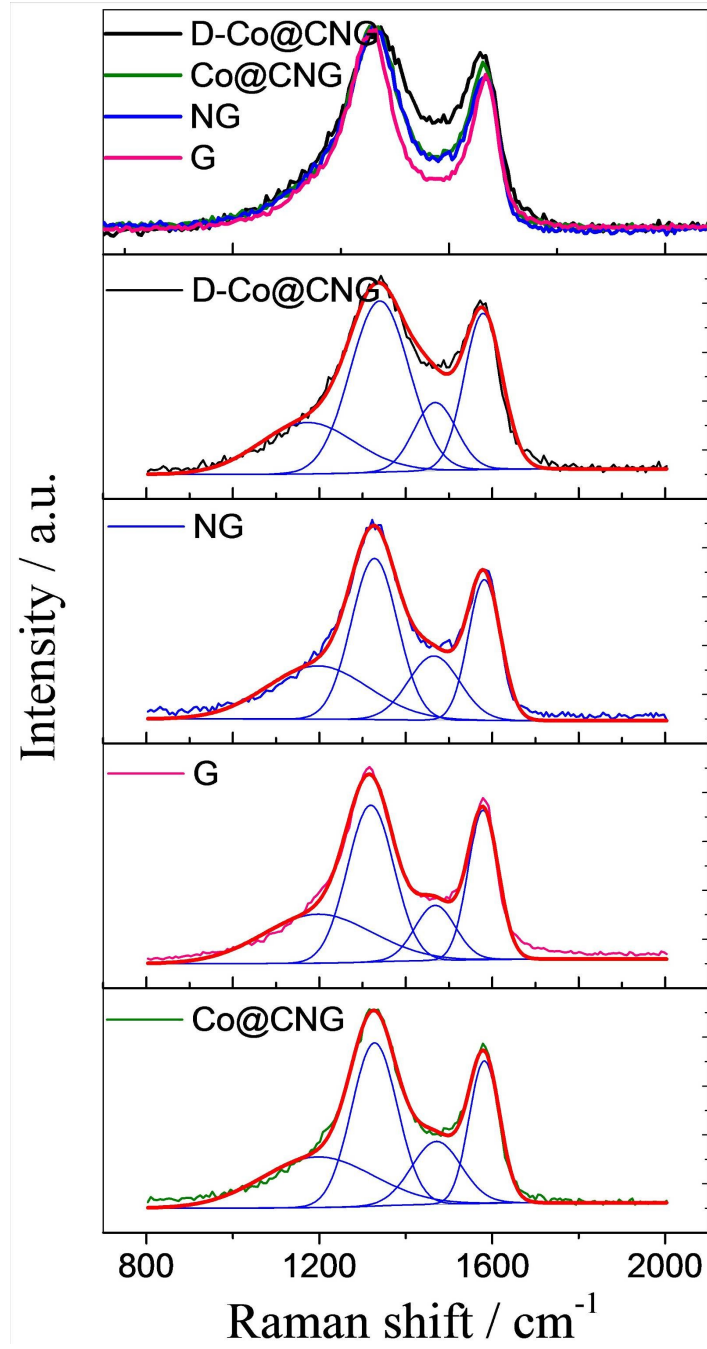


Figure 9. Raman spectra of D-Co@CNG, Co@CNG, NG and G and the deconvolution at D and G bands.

Table 2. The peak fitting parameters of D-Co@CNG, NG, G and Co@CNG from Raman spectra in Figure 9.

	Intensity percentage of peak I (1170 cm ⁻¹)	Intensity percentage of peak II (1337 cm ⁻¹)	Intensity percentage of peak III (1473 cm ⁻¹)	Intensity percentage of peak IV (1583 cm ⁻¹)	Peak II /Peak IV (I _D /I _G)
D-Co@CNG	11.49	38.33	15.25	34.93	1.10
Co@CNG	12.09	38.92	15.02	33.97	1.15
NG	12.70	38.43	15.30	33.57	1.14
G	12.39	38.07	13.66	35.88	1.06

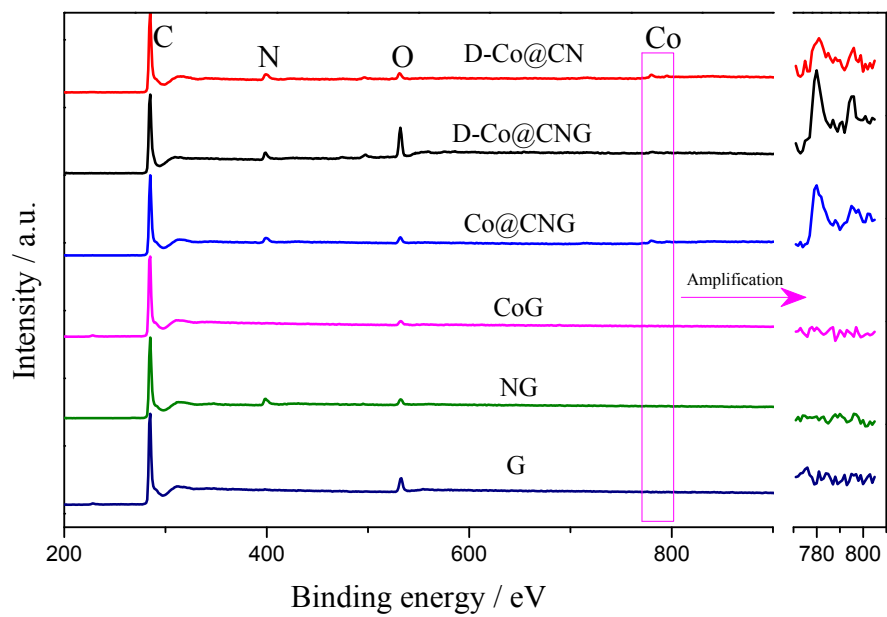


Figure 10. X-ray photoelectron spectroscopy (XPS) spectra (left) of D-Co@CNG, D-Co@CN, Co@CNG, NG, CoG and G and their corresponding Co regions (right).

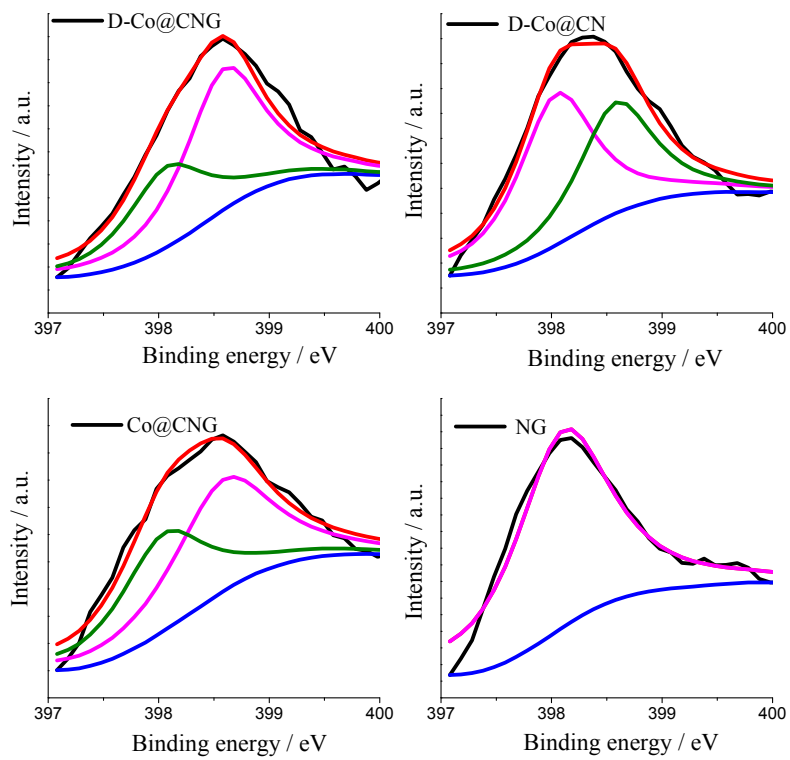


Figure 11. Deconvolution of high-resolution pyridinic N 1s XPS spectra on different materials.

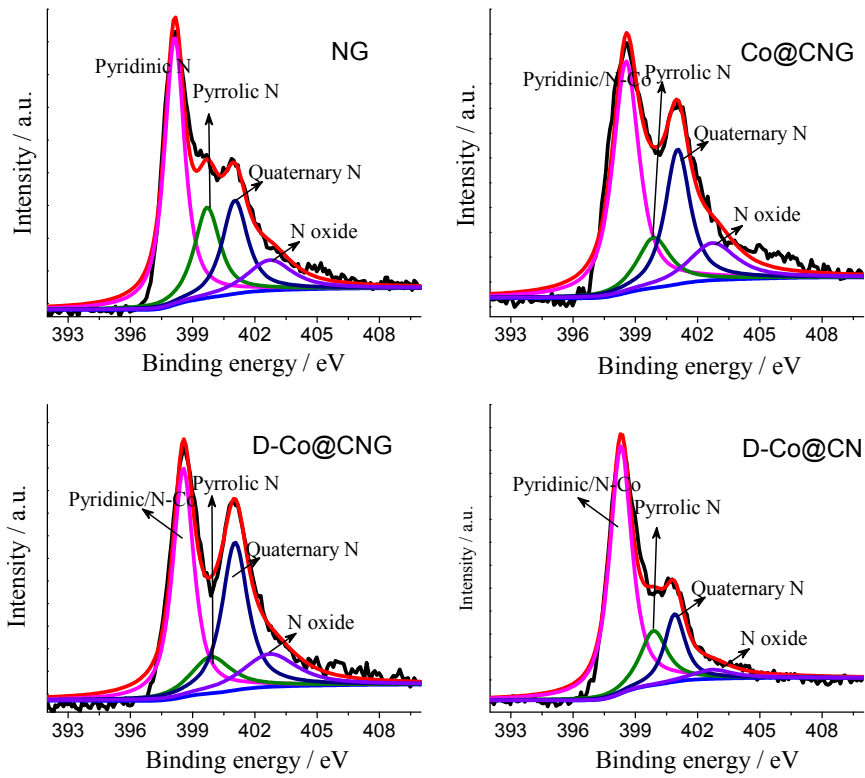


Figure 12. Deconvolution of high-resolution N 1s XPS spectra on different materials.

Table 3. Contents of Co and N in Co@CNG, CoG, NG, D-Co@CN and D-Co@CNG as determined by XPS analysis.

	Co content (wt.%)	Overall N content (wt.%)	N content from N-Co (wt.%)
Co@CNG	2.52	6.45	1.70
NG	--	7.80	--
D-Co@CN	1.54	6.75	2.48
D-Co@CNG	3.00	7.20	1.83

Table 4. Contents of different types of N in Co@CNG, NG, D-Co@CN and D-Co@CNG as determined by XPS analysis.

	pyridinic	pyrrolic	quaternary	oxidized	Pyridinic+ quaternary
Co@CNG	3.03	0.84	1.70	0.88	4.73
NG	3.66	1.58	1.61	0.94	5.27
D-Co@CN	4.25	1.15	1.07	0.27	5.32
D-Co@CNG	2.91	0.90	2.31	1.08	5.22

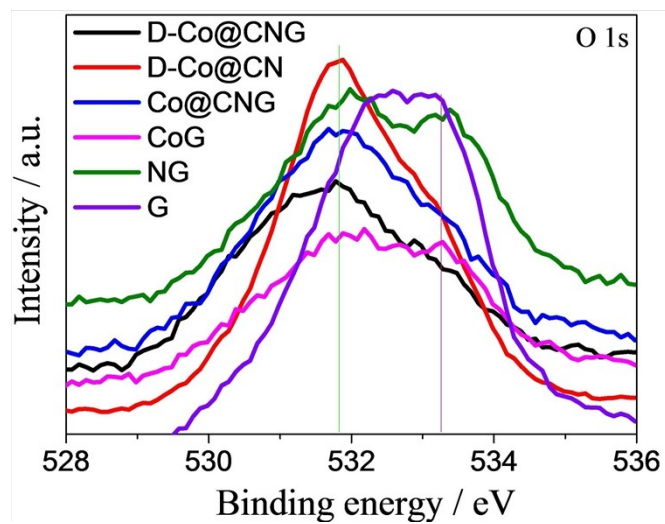


Figure 13. High-resolution O1s XPS spectra of different materials.

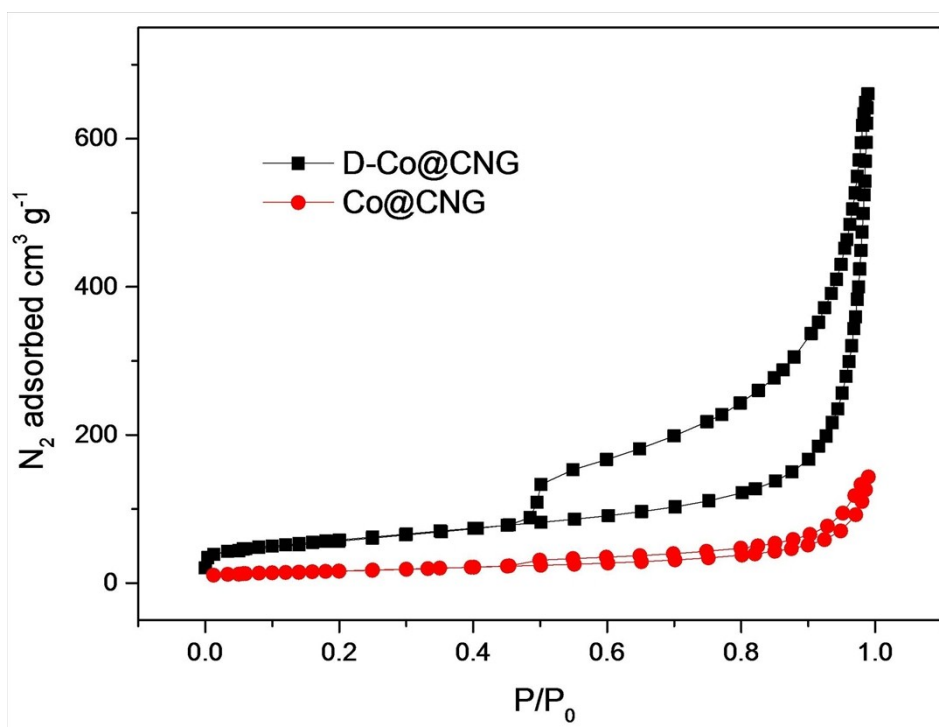


Figure 14. Nitrogen adsorption/desorption isotherms of D-Co@CNG and Co@CNG.

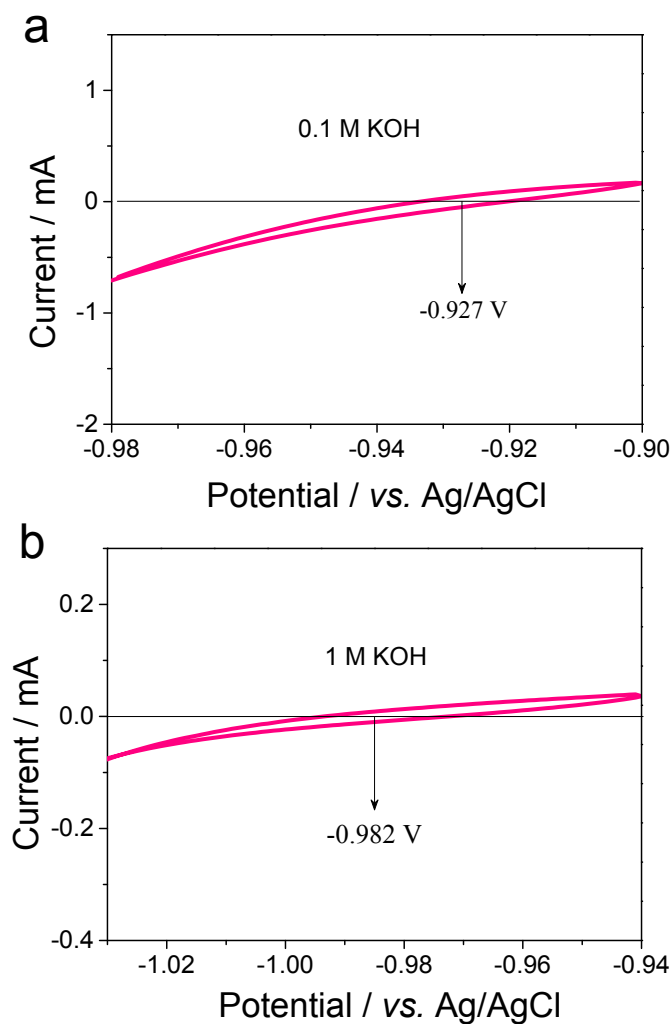


Figure 15. Potential calibration of the reference electrode in 0.1 M and 1 M KOH solutions.

RHE calibration: Ag/AgCl/KCl was used as the reference electrode in all the measurements. It was calibrated with respect to reversible hydrogen electrode (RHE). The calibration was performed in the hydrogen saturated electrolyte with a Pt mesh as the working electrode. CVs were carried out at a scan rate of 2 mV s^{-1} , and the average value of the two potentials at which the current crossed zero was taken to be the thermodynamic potential for the hydrogen electrode reactions.

$$E_{(\text{RHE in } 0.1 \text{ M KOH})} = E_{(\text{Ag/AgCl})} + 0.927 \text{ V}$$

$$E_{(\text{RHE in } 1 \text{ M KOH})} = E_{(\text{Ag/AgCl})} + 0.982 \text{ V}$$



Figure 16. Schematic diagram of intermedia transform on the disk and ring during HER, OER and ORR.

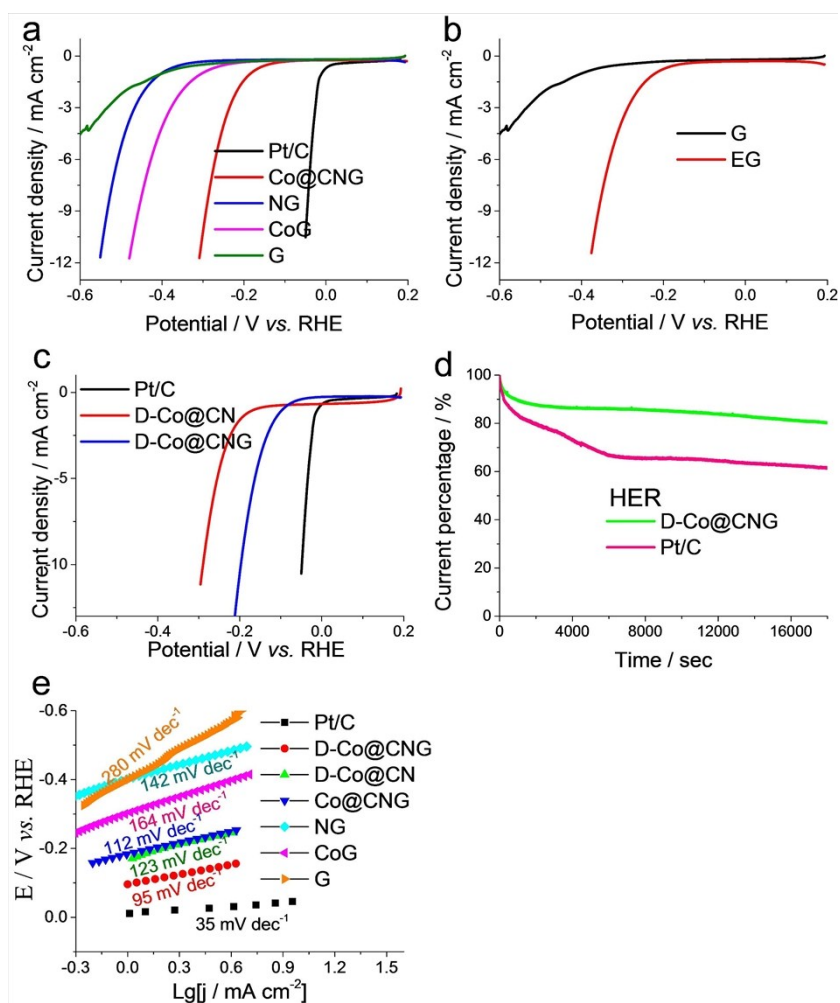


Figure 17. (a-c) HER LSV curves for the Pt/C (20%), D-Co@CNG, D-Co@CN, Co@CNG, NG, CoG, G and EG in 1 M KOH (scan rate of 10 mV s^{-1}); (d) Chronoamperometric responses of the D-Co@CNG and Pt/C (20 wt.%); (e) Tafel plots of different catalysts in 1 M KOH.

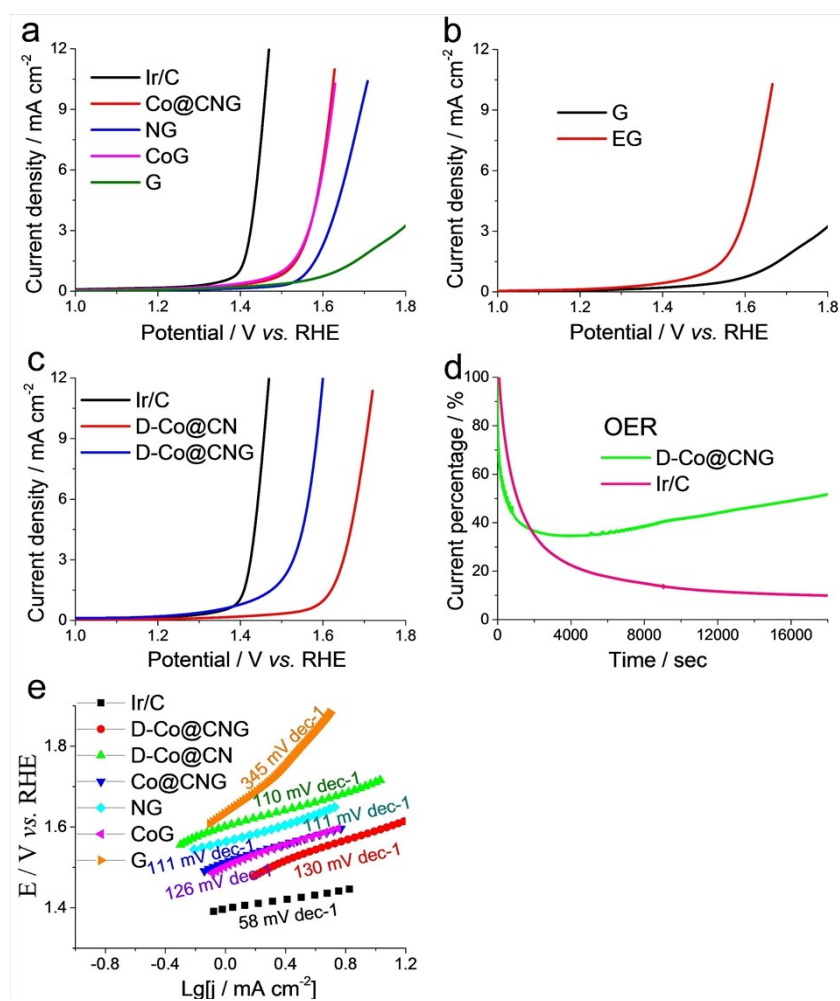


Figure 18. (a-c) OER LSV curves for the Ir/C (20%), D-Co@CNG, D-Co@CN, Co@CNG, NG, CoG, G and EG in 1 M KOH (scan rate of 10 mV s^{-1}); (d) Chronoamperometric responses of the D-Co@CNG and Ir/C (20 wt.%); (e) Tafel plots of different catalysts in 1 M KOH.

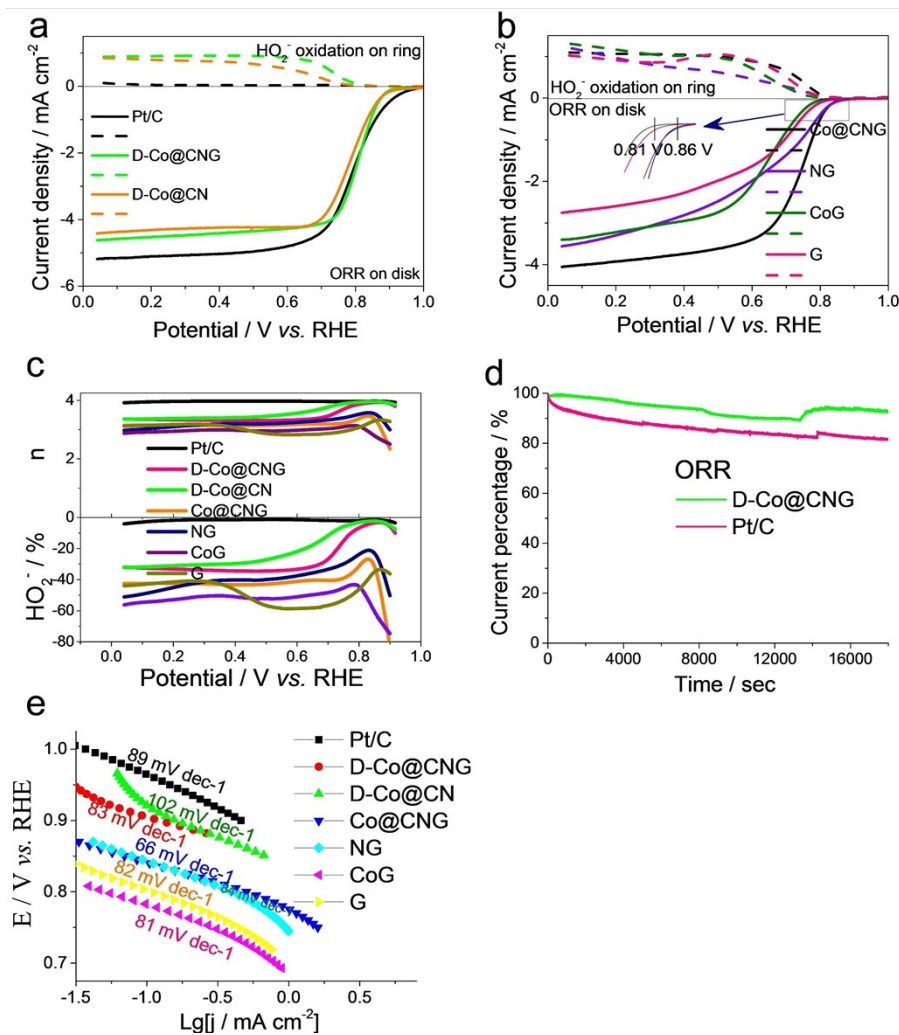


Figure 19. (a-b) RRDE measurements of O_2 reduction on Pt/C (20%), D-Co@CNG, D-Co@CN, Co@CNG, NG, CoG and G in 0.1 M KOH (scan rate of 5 mV s^{-1}). The Pt-ring electrode was maintained at 1.40 V for the oxidation of the HO_2^- that was evolving on the disk electrode. (c) Percentage of peroxide in the total oxygen reduction products and the number of electron transfer. (d) Chronoamperometric responses of the D-Co@CNG and Pt/C (20%). (e) Tafel plots of different catalysts in 0.1 M KOH.

On the basis of the RRDE results, the electron transferred number (n) and the percentage of HO_2^- generated during the oxygen reduction were calculated by using the followed equations:³ where I_d is disk current, I_r is ring current, and N is current

collection efficiency of the Pt ring. N was determined to be 0.40 from the reduction of



$$n = 4 \frac{I_d}{I_d + I_r / N} \quad \text{HO}_2^- = 200 \frac{I_r / N}{I_d + I_r / N}$$

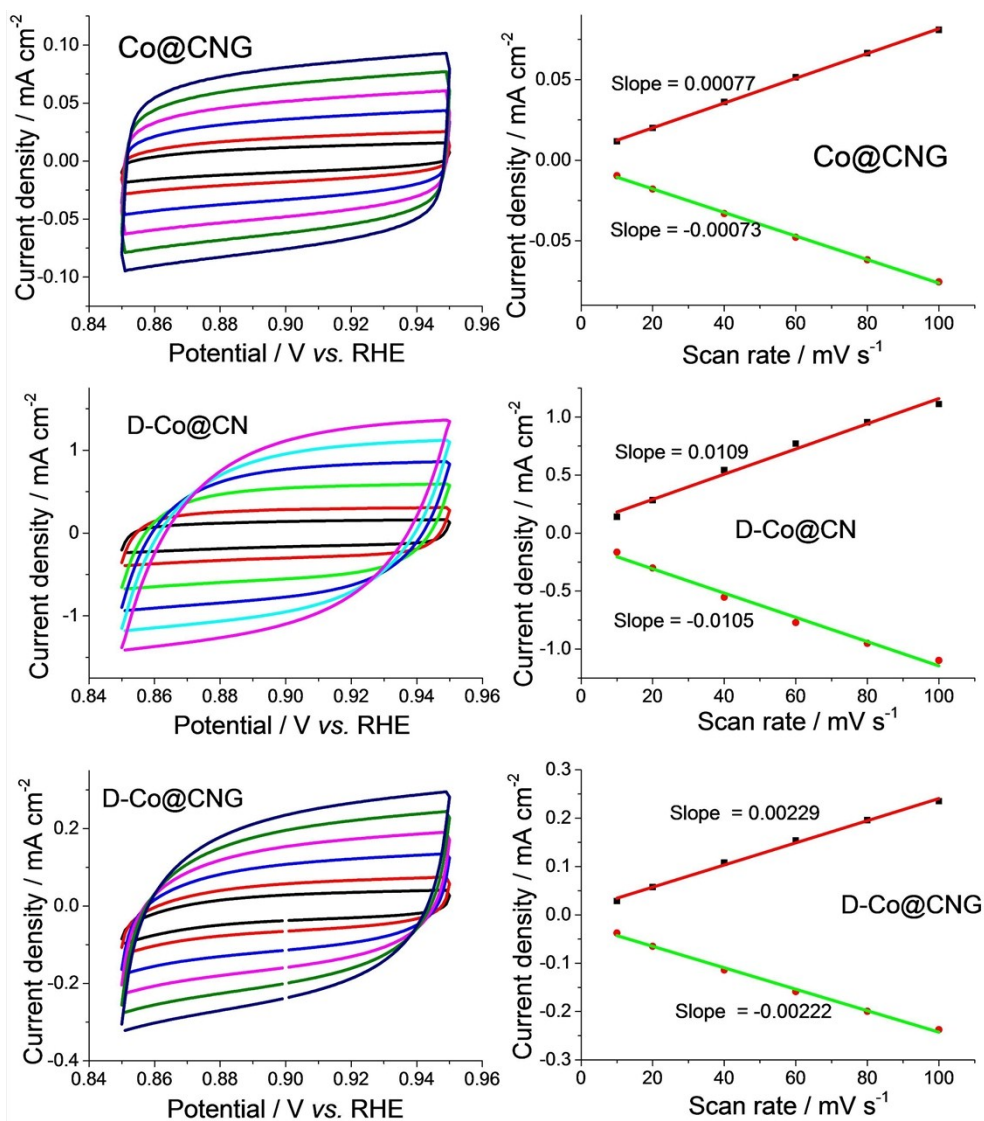


Figure 20. Double-layer capacitance measurements for determining the electrochemical active surface area of Co@CNG, D-Co@CN and D-Co@CNG. (a1, b1 and c1) CVs measured in a non-Faradaic region at scan rate of 10 mV s^{-1} , 20 mV s^{-1} , 40 mV s^{-1} , 60 mV s^{-1} , 80 mV s^{-1} , and 100 mV s^{-1} . (a2, b2 and c2) The cathodic (red) and anodic (green) currents measured at 0.9 V vs RHE as a function of the scan rate. The average of the absolute value of the slope is taken as the double-layer capacitance of the electrode.

The ECSA for the Co-NG electrode with mass loading of 0.2 mg cm⁻² was estimated from the electrochemical double-layer capacitance (C_{dl}) of the catalytic surface. The C_{dl} was determined from the scan-rate dependence of CVs in a potential range where there is no Faradic current. The results were shown in Figure 20, which yields C_{dl}. The ECSA can be calculated from the C_{dl} according to:

$$ECSA = \frac{C_{dl}}{C_s} \quad (3)$$

where C_s is the specific capacitance of a flat standard electrode with 1 cm² of real surface area, which is generally in the range of 20 to 60 μF cm⁻². If we use the averaged value of 40 μF cm⁻² for the flat electrode,⁵ we obtain:

$$ECSA = \frac{C_{dl}}{C_s} = \frac{mF \text{ cm}^{-2}}{40 \mu F \text{ cm}^{-2} \text{ per cm}_{ECSA}^2} = cm_{ECSA}^2 \quad (4)$$

$$C_{dl}(\text{Co@CNG}) = 0.75 \text{ mF cm}^{-2} \quad ECSA(\text{Co@CNG}) = 18.75 \text{ cm}^2$$

$$C_{dl}(\text{D-Co@CN}) = 10.7 \text{ mF cm}^{-2} \quad ECSA(\text{D-Co@CN}) = 267.5 \text{ cm}^2$$

$$C_{dl}(\text{D-Co@CNG}) = 2.3 \text{ mF cm}^{-2} \quad ECSA(\text{D-Co@CNG}) = 57.5 \text{ cm}^2$$

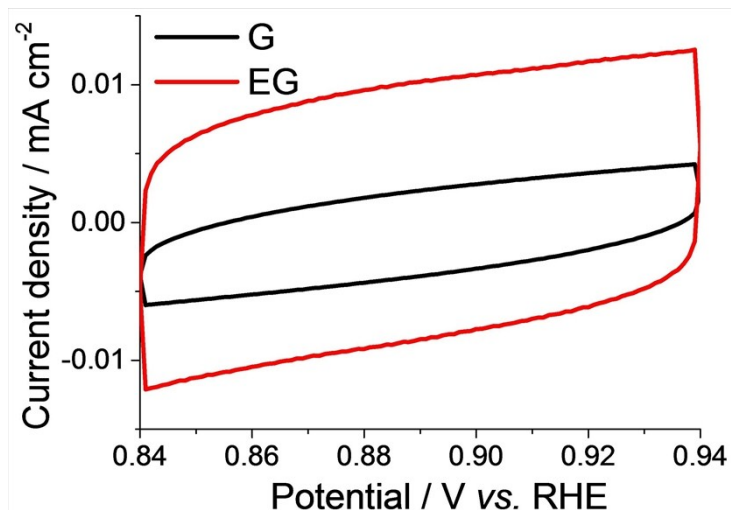


Figure 21. Double-layer measurements at 10 mV s^{-1} for the G and EG.

EG shows better catalytic activities relative to G as indicated by Figure 17b and 18b. Note that direct pyrolysis of GO (synthesis for EG) experienced an explosion process, during which the pyrolysis gas such as H_2O and/or other gaseous organics was released fiercely at the elevated temperature, leading to the explosion process. As a result of the similar composition and structure, we assume that EG possess a higher ECSA relative to G. Double-layer measurement in Figure 21 clearly confirm this hypothesis.

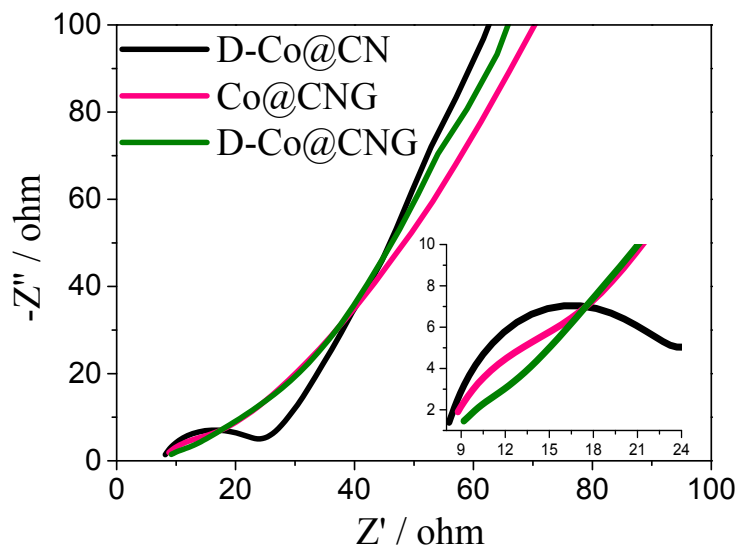


Figure 22. Electrochemical impedance spectroscopies (EISs) of D-Co@CN, Co@CNG and D-Co@CNG.

In Figure 22, the three catalysts show similar solution resistance as determined by the intercept on the Z' axis of ca. 8.8Ω . The charge transfer resistance of D-Co@CN can be evaluated by the numerical value of the diameter of the semicircle on the Z' axis,⁶ which is obviously larger than the other two catalysts. D-Co@CNG shows very small charge transfer resistance as witnessed by the nearly disappeared semicircle in the inset in Figure 22. The inclined lines in the low frequency are attributed to the Warburg impedance, which is in association with ion diffusion in the electrode materials. The slope values of the inclined lines are proportional to the ion diffusion coefficient.⁷ As can be seen, a higher diffusion coefficient of the D-Co@CNG catalyst, which is close to D-Co@CN, represents the higher mobility for ions diffusion as compared to Co@CNG.⁸ The lowest charge transfer resistance on D-Co@CNG indicates the excellent electronic conductivity after incorporation with graphene. Furthermore, the properly high ion diffusion coefficient suggests high ion

transfer speed across interfaces from the electrolyte to active electrode materials.^{8,9}

Both impart the high electrocatalytic performance.

Table 5. Comparison in HER performance of some multifunctional catalysts reported recently in literature.

Source/References	Solution	Loading (mg cm ⁻²)	Tafel slope value mV dec ⁻¹	Onset overpotential (mV)	Overpotential at 10 mA cm ⁻² (mV)
<i>This work (D-Co@CNG)</i>	1 M KOH	0.20	95	57	205
<i>Adv. Mater.</i> 2017, 1604942 (SHG)	0.1 M KOH	0.20	112	230	310
<i>Adv. Funct. Mater.</i> 2015, 25, 5799–5808 (i. Ni-NiO/N-rGO (ii. Co-CoO/N-rGO)	0.1 M KOH	0.21	<i>i.46</i> <i>ii.51</i>	<i>i.20</i> <i>ii.40</i>	<i>i.145</i> <i>ii.155</i>
<i>Adv. Funct. Mater.</i> 2015, 25, 872–882 (N/Co-doped PCP//NRGO)	0.5 M H ₂ SO ₄	0.35	126	100	229
<i>Angew. Chem.</i> 2016, 128, 13490–13494 (N, P, and F tri-doped graphene)	0.1 M KOH	Not mentioned	--	400	520
<i>Adv. Mater.</i> 2016, 28, 9532–9538 (Defect Graphene)	1 M KOH	0.28	118	200	340
<i>Chem. Commun.</i> , 2016, 52, 5946–5949 (Co/CoO@Co-N-C)	0.1 M KOH	0.3	--	~200	~330
<i>J. Mater. Chem. A</i> , 2016, 4, 17288–17298 (Co@NCNT)	0.1 M KOH	0.42	--	~100	~240

Note: SHG stands for stereoscopic holes over the graphene. ~ stands for the data obtained from the Figures in the literature. All the potentials are calibrated and converted to reversible hydrogen electrode.

Table 6. Comparison in OER performance of some multifunctional catalysts reported recently in literature.

Source/References	Solution	Loading (mg cm ⁻²)	Tafel slope value mV dec ⁻¹	Onset overpotential (mV)	Overpotential at 10 mA cm ⁻² (mV)
<i>This work (D-Co@CNG)</i>	1 M KOH	0.20	130	230	360
<i>Adv. Mater.</i> 2017, 1604942 (SHG)	0.1 M KOH	0.20	71	260	370
<i>Adv. Funct. Mater.</i> 2015, 25, 5799–5808 (i.Ni-NiO/N-rGO) (ii.Co-CoO/N-rGO)	0.1 M KOH	0.21	<i>i.43</i> <i>ii.68</i>	<i>i.140</i> <i>ii.290</i>	<i>i.230</i> <i>ii.400</i>
<i>Adv. Funct. Mater.</i> 2015, 25, 872–882 (N/Co-doped PCP//NRGO)	0.1 M KOH	0.35	--	~240	430
<i>Angew. Chem.</i> 2016, 128, 13490–13494 (N, P, and F tri-doped graphene)	0.1 M KOH	Not mentioned	136	390	470
<i>Adv. Mater.</i> 2016, 28, 9532–9538 (Defect Graphene)	1 M KOH	0.28	97	~230	340
<i>Chem. Commun.</i> , 2016, 52, 5946–5949 (Co/CoO@Co-N-C)	0.1 M KOH	0.3	--	~330	~410
<i>J. Mater. Chem. A</i> , 2016, 4, 17288–17298 (Co@NCNT)	1 M KOH	0.42	116	~370	~430

Note: SHG stands for stereoscopic holes over the graphene. ~ stands for the data obtained from the Figures in the literature. All the potentials are calibrated and converted to reversible hydrogen electrode.

Table 7. Comparison in ORR performance of some multifunctional catalysts reported recently in literature.

Source/References	Solution	Loading (mg cm ⁻²)	Half-wave potential (V) (E _{1/2} vs RHE)	Tafel slope value mV dec ⁻¹	Activity vs. Pt/C
<i>This work</i> (D-Co@CNG)	0.1 M KOH	0.20	0.81	83	comparable
<i>Adv. Mater.</i> 2017, 1604942 (SHG)	0.1 M KOH	0.20	0.87	--	comparable
<i>Adv. Funct. Mater.</i> 2015, 25, 5799–5808 (Co-Co/N-rGO)	0.1 M KOH	0.21	0.75	40	worse
<i>Adv. Funct. Mater.</i> 2015, 25, 872–882 (N/Co-doped PCP//NRGO)	0.1 M KOH	0.7	0.86	85	comparable
<i>Angew. Chem.</i> 2016, 128, 13490–13494 (N, P, and F tri-doped graphene)	0.1 M KOH	Not mentioned	0.75	--	worse
<i>Adv. Mater.</i> 2016, 28, 9532–9538 (Defect Graphene)	0.1 M KOH	0.08	0.76	76	worse
<i>Chem. Commun.</i> , 2016, 52, 5946–5949 (Co/CoO@Co–N–C)	0.1 M KOH	0.3	~0.82	--	comparable
<i>J. Mater. Chem. A</i> , 2016, 4, 17288–17298 (Co@NCNT)	0.1 M KOH	0.425	~0.84	95	comparable

Note: SHG stands for stereoscopic holes over the graphene. ~ stands for the data obtained from the Figures in the literature. All the potentials are calibrated and converted to reversible hydrogen electrode.

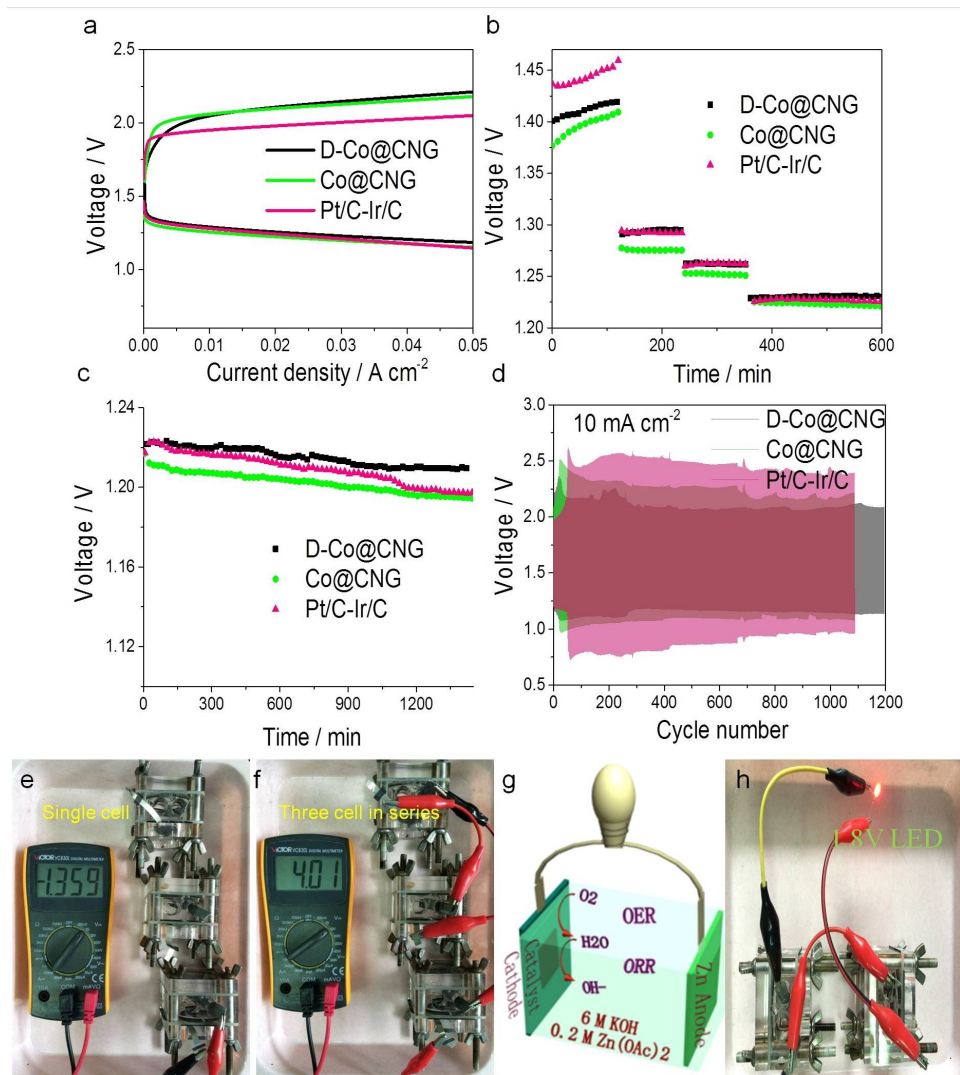


Figure 23. (a) Charge and discharge polarization curves of Zn–air batteries using D-Co@CNG, Co@CNG or Pt/C-Ir/C catalyst as air electrodes. (b) Rate performance of different Zinc-air batteries using D-Co@CNG, Co@CNG or Pt/C-Ir/C catalyst as air electrode. (c) Discharge performance at 10 mA cm^{-2} for 24 h for calculation of Coulombic efficiency. (d) Discharge/charge cycling curves of two-electrode rechargeable Zn–air batteries at a current density of 10 mA cm^{-2} using the D-Co@CNG, Co@CNG or Pt/C-Ir/C air electrodes. (e-f) Photograph of open circuit voltage with single battery and three batteries in series (after 1000 discharge/charge cycles at 5 mA cm^{-2}). (g) Schematic representation of the basic configuration of a two-

electrode Zn–air battery by coupling the Zn electrode with a air electrode to execute ORR and OER. (h) Photographs of a red LED (1.8 V) powered by two Zn-air batteries integrated in series (after cycles).

For the calculation of Coulombic efficiency in Figure 17c, the mass loss of Zn by using D-Co@CNG, Co@CNG and Pt/C-Ir/C electrodes in Zn-air batteries is 312.6, 321.9, 311.5 mg, respectively. Thus the theoretical output Coulomb for D-Co@CNG, Co@CNG and Pt/C-Ir/C electrodes should be 922.6, 950.1 and 919.4 C, respectively. The actual output Coulomb is $10\text{mA} \times 24\text{h} \times 3600/1000=864$ C.

Therefore, we can get the Coulombic efficiency for D-Co@CNG, Co@CNG and Pt/C-Ir/C electrodes is 93.6%, 90.9% and 94.0%, respectively.

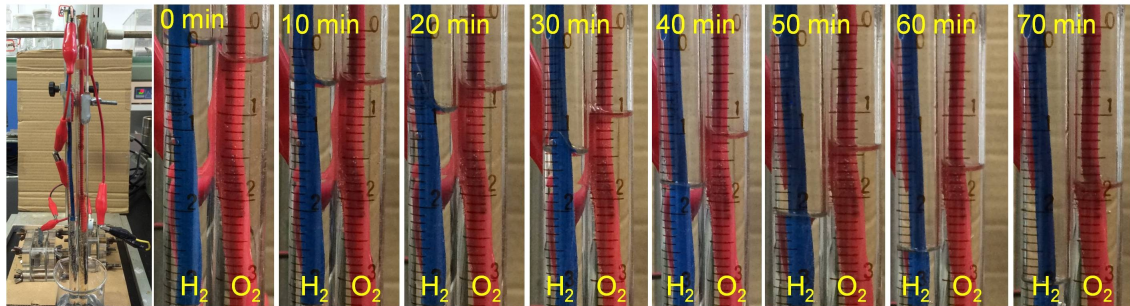


Figure 24. The optical images of the O₂ and H₂ collection tubes at various splitting times powered by two batteries in series.

For the calculation of Faradaic efficiency during long-term electrolysis (about 24 h): The practical volume of H₂ and O₂ after electrolysis determined to be 50.0 and 24.5 ml, respectively. The corresponding average mass loss of Zn (99.99%) was 146.35 mg. Thus we can get the Faradaic efficiency for H₂ and O₂ is 99.8% and 97.6%, respectively.

References:

1. S. Zhang, L. Zhu, H. Song, X. Chen, B. Wu, J. Zhou, F. Wang, *J. Mater. Chem.* **2012**, *22*, 22150.
2. D. C. Marcano, D. V. Kosynkin, J. M. Berlin, A. Sinitskii, Z. Sun, A. Slesarev, L. B. Alemany, W. Lu, J. M. Tour, *ACS Nano* **2010**, *4*, 4806.
3. Y. Li, W. Zhou, H. Wang, L. Xie, Y. Liang, F. Wei, J.-C. Idrobo, S. J. Pennycook, H. Dai, *Nat. Nano.* **2012**, *7*, 394.
4. C. Paliteiro, A. Amnett, J. B. Goodenough, *J. Electroanal. Chem. Interfacial Electrochem.* **1987**, *233*, 147.
5. H. Fei, J. Dong, M. J. Arellano-Jiménez, G. Ye, N. D. Kim, E. L.G. Samuel, Z. Peng, Z. Zhu, F. Qin, J. Bao, M. J. Yacaman, P. M. Ajayan, D. Chen, J. M. Tour, *Nat. Commun.* **2015**, *6*, 8668.
6. C. Hu, Y. Xiao, Y. Zhao, N. Chen, Z. Zhang, M. Cao, L. Qu, *Nanoscale* **2013**, *5*, 2726.
7. Y.-S. Hu, P. Adelhelm, B. M. Smarsly, S. Hore, M. Antonietti, J. Maier, *Adv. Funct. Mater.* **2007**, *17*, 1873.
8. X. Wu, Q. Liu, Y. Guo, W. Song, *Electrochem. Commun.* **2009**, *11*, 1468.
9. G. Zou, D. Zhang, C. Dong, H. Li, K. Xiong, L. Fei, Y. Qian, *Carbon* **2006**, *44*, 828.